Submitted to the 1995 IEEE International Conference on Robotics and Automation

# Fourier Analysis of the Bandlimited Shape Estimation Problem in Tactile Sensing*

Edward J. Nicolson and Ronald S. Fearing
Department of EE&CS
University of California
Berkeley, CA 94720

## Abstract

*This paper focuses on static sensing of local contact shape from passive touch through the use of a capacitive array sensor embedded in an elastic medium. Previously we have determined sensor spacing requirements given sensor depth and developed techniques for determining the Fourier coefficients for a pressure distribution given indenter shape [15]. By comparing line load frequency responses for sensors at different depths with the Fourier representations of indenter pressure distributions, we determine the sensor depth at which shape classification and discrimination is possible. The results indicate that our current sensor designs allow shape discrimination within a class but not differentiation between indenter classes.*

## 1 Introduction

Recently it has been shown that the human tactile sensory system is capable of fine shape discrimination from static touch [7]. Robotic tactile sensors have also been shown to have the capability of providing curvature information [5], however recent results using finite-element models of tactile sensors indicate that shape classification is hard [3]. Since it is already known that the rubber layer on the finger acts as a spatial low pass filter and that the frequency of the filter cut-off decreases as sensor depth increases [4, 15, 19], this paper investigates the shape sensing capabilities of tactile sensors as a function of the sensor depth.

We can motivate the study of static tactile sensing with results from neurophysiological research. It is often assumed that fine shape discrimination requires active touch, however a couple of results indicate otherwise. In 1969 Vierck showed that although the two point threshold on the arm indicated apparently poor static spatial sensitivity, the ability to estimate the diameter of an indenter was actually quite good. He showed that with a two point threshold of 30 mm, indenters varying in diameter as little as 4 mm could be distinguished. For most of the test stimuli this corresponded roughly to a difference in diameter of 25 %. If one assumed that this 7.5 times scaling relationship between the two point threshold and indenter diameter was maintained on the finger tip then humans would have the ability to discriminate diameters varying as little as 0.3 mm from a nominal diameter of 1.2 mm.

Recently Goodwin conducted experiments to determine the ability of humans to discriminate spheres of varying radii pressed into human fingerpads at various loads after a period of training [7]. It was found that, at a 75 % level, humans could discriminate between a flat surface and a radius of 204 mm, and between a radius of 6.95 mm and 6.17 mm, a difference of 12.5 %. Interestingly enough, this corresponds to a change in diameter of contact area of 0.6 mm.

For comparison, humans are able to discriminate between a flat surface and a radius of 550 mm when they are allowed to move their fingers over the surface of the object [8]. Perhaps the most important difference between these two studies is training. Static discrimination of curvature improved with training, but haptic discrimination did not require training. We can conclude that the human sensory system has the *capability* of statically discriminating curvatures.

Most robotic tactile sensors, utilizing similar sensor densities to that of humans, have not demonstrated as fine a shape discrimination ability. In most cases analysis of their performance has been limited to sensitivity of a single cell and their ability to produce "touch pictures". Techniques from machine vision such as moment analysis [13, 21, 18, 9, 12] and edge detection [1, 2, 20] are often applied to these images. With a high resolution tactile sensor and a Hertz contact

*This work was funded in part by: NSF Grant IRI-9114446, NSF-PYI grant IRI-9157051, and a National Needs Fellowship.

model it is possible to estimate the radius of a cylinder using machine vision techniques [18]. For the foam rubber used in [18] loads greater than 20 N were required to estimate the diameter of a 41 mm cylinder with a standard error of 2.2 mm.

The main problem with using machine vision techniques is that they are not well adapted to the low resolution typically afforded by tactile sensors. In vision the problem is information reduction, or, finding a feature in a high resolution array of pixels. To use machine vision techniques it is first necessary to invert the spatial low pass filter due to the rubber layer so as to reconstruct a higher resolution surface image and then threshold that image to find edges in it [2]. This technique leads to noise amplification, and assumes the the sampled array is just a low pass filtered version of the normal surface *displacement* when in fact the sampled data is due to both normal and shear tractions on the surface.

Another approach is to develop tactile sensor data analysis techniques based on the mechanics of the rubber material in which they are usually embedded. In [6, 4, 5] it is shown how the linear elastic half space model can be used to determine contact location, curvature, orientation, and force from subsurface normal strain data on a cylindrical finger. One of the key points of this work was that fine position and curvature information could be obtained from a very low sensor densities by using appropriate models.

As an alternative to subsurface strain sensing, it has been suggested that surface displacement sensing would provide better shape estimates since the data is not spatially filtered. By comparing the interpolated response of the surface displacement sensors of Hutchings [10] (resolution 6.8 microns), and sub-surface strain sensors of Fearing [4] (resolution 0.1 %strain) at the same density of 0.31 $\frac{1}{\mathrm{mm}^2}$, one can see a possible indenter discrimination problems with displacement sensors. As is shown in Figure 1, the displacement sensor can potentially misinterpret a knife edge as a round indenter due to the high degree of aliasing in interpolation. In addition the response of the displacement sensor is only 2 quantization units while the sampled strains are at 6 times the quantization level. If the contact is moved by half a sensor spacing the displacement sensor output will change dramatically. The peak of the interpolated profile will appear to change from 20 microns to 200 microns (1000 %). The peak of the strain profile will change by 15 %. Shortly we will review the strain and displacement knife edge frequency response to see the cause of this effect.

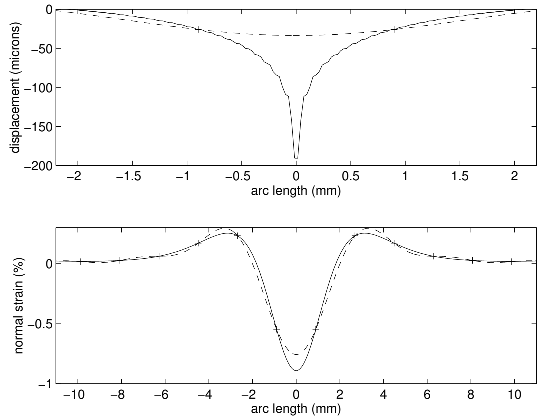


Figure 1: *A knife edge indented into an elastic sensor directly between displacement (top) and strain (bottom) sensors. The crosses indicate sensor locations and the dashed lines are the result of sinc interpolation of the samples.*

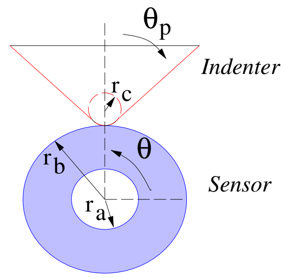


Figure 2: *Sensor radii parameters and indenter shape as a function of $\theta_p$ and $r_c$. In the contact region the deformed profile of the sensor must match that of the rigid indenter.*

We proceed by reviewing the linear elastic model introduced in [15] and then use the model to determine limits of shape sensing based on sensor depth.

## 2 Linear elastic tactile sensor model

Under the assumptions of material linearity, isotropy, and homogeneity, the problem of determining indenter shape, location, and total load from subsurface strain measurements on a tactile sensor may be analyzed with linear elasticity. Previously we developed a model for a cylindrical geometry sensor which we will review here [15].

First we review the sensor and indenter geometry as is shown in Figure 2. The cylindrical sensor has a solid core of radius $r_a$. An annulus of rubber is molded around the core with an outer radius of $r_b$. $n_s$ sensors are evenly placed within the rubber at a radius $r_s$, $r_a < r_s < r_b$. An indenter touches the finger at

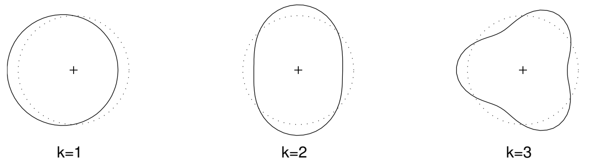


Figure 3: *Fourier series basis.*

location $\theta$. The radius of curvature of the indenter is $r_c$ and its half angle is $\theta_p$. For round indenters $\theta_p$ is small, for wedge indenters $r_c$ is small and the half angle of the wedge is $\theta_p$. By picking $\theta_p$ and $r_c$ appropriately a continuum from wedge indenters to rounded indenters can be constructed.

A number of derived parameters will also be discussed.

$$\alpha = \frac{r_a}{r_b} \quad , \quad \gamma = \frac{r_s}{r_b} \quad , \quad \frac{1}{R} = \frac{1}{r_b} + \frac{1}{r_c}$$

For round indenters, where $\theta_p$ is small, the composite radius, $R$, can be interpreted as the equivalent radius of the indenter if the sensor were flat.

## 2.1 Fourier series decomposition

As we are using linear elasticity to solve this problem we may use the principle of superposition to sum independent partial solutions. The sum of these partial solutions gives the desired solution. Since all the partial solutions will be periodic in $\theta$ with period $2\pi$, a Fourier series decomposition is natural. We will denote normal radial stress by $\tau_{rr}$, radial displacement by $u_r$, and radial normal strain by $e_{rr}$. At $r_b$, the normal surface stress will be given by $p(\theta)$. Using a trigonometric Fourier series we can write the surface tractions as follows

$$\tau_{rr}(r_b, \theta) = p(\theta) = p_0 + \sum_{k=1}^{\infty} p_k^c \cos k\theta + \sum_{k=1}^{\infty} p_k^s \sin k\theta$$

We desire a solution of the form

$$e_{rr}(r, \theta) \quad = \quad e_{rr_0}(r) + \sum_{k=1}^{\infty} e_{rr_k}^c(r) \cos k\theta + \sum_{k=1}^{\infty} e_{rr_k}^s(r) \sin k\theta.$$

The solution to this linear elastic problem for the boundary conditions of zero stress outside the contact region at $r_b$ and zero displacement at $r_a$ is given in [15].

Figure 3 shows the first 3 components of the Fourier series decomposition for radial displacements. We will now use this Fourier based model to analyze the problem of determining shape from low frequency information otherwise known as the problem of *bandlimited shape interpretation.*

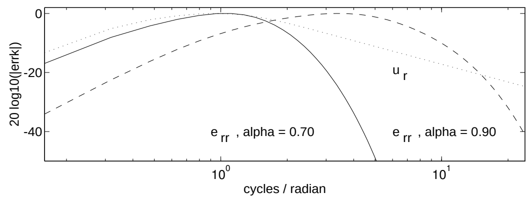


Figure 4: *Line load frequency response for normal surface displacement (dotted line) and subsurface strain at two different depths (solid and dashed lines).*

## 2.2 Frequency response

The line-load normal-strain frequency response determines which spatial frequencies will be sensed by the tactile sensor for a given set of radii: $r_a$, $r_s$, and $r_b$. Figure 4 shows the strain and displacement frequency responses in a conventional Bode plot. Before going on to discuss strain measurements, notice first that the displacement frequency response decays very close to that of a one pole low pass filter at 20 dB/decade while the strain response decays much faster at more than 100 dB/decade. We also know that one pole low pass filters are not very good anti-aliasing filters. On the other hand the subsurface strain responses show that they are very good low pass filters. Thus from a filter design point of view, one would much rather use subsurface strain measurements since the strain field has a well defined frequency content whereas the frequency content of the displacement field is not clearly bandlimited.

For the remainder of the discussion of shape interpretation we will be comparing two sensor designs, one with deep sensors with $\alpha = 0.70$ and $\gamma = 0.74$ and the other design with shallow sensors with $\alpha = 0.90$ and $\gamma = 0.96$. From Figure 4 we see that the deep sensors have a -40 dB cut-off at 4.5 cycles/radian while the shallow sensors have their cut-off at 25 cycles/radian.

## 2.3 Comparison of indenter classes

Using a singular value decomposition technique discussed in [15], the Fourier coefficients of the pressure distribution for an arbitrary indenter shape can be computed. We use this technique to explore representations of different indenters in the Fourier domain.

The displacement, surface pressure, and subsurface strain fields for three different indenter classes were compared. Indenters were compared that had both the same load and contact area so as to generate as similar as possible sub-surface strain profiles. A 10 mm cylinder, a 166 degree wedge, and a flat punch all generate a 3 mm contact area at 200 N/m. Figure 5 shows the displacement field, pressure distribution, and subsurface strain at two depths for the three

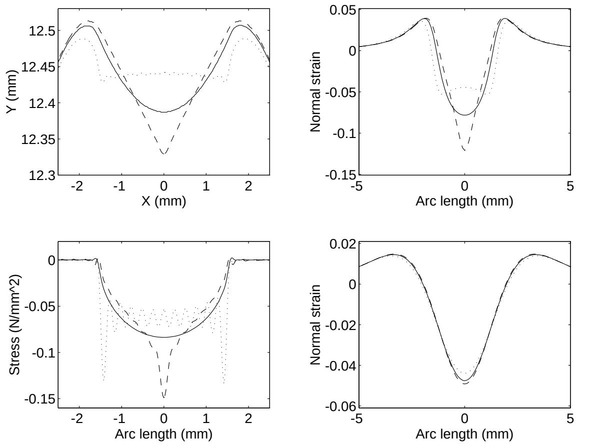


Figure 5: *Comparison of indenter classes for a round indenter (solid line), a wedge indenter (dashed line), and a punch indenter (dotted line) which all have the same contact area and total load. Upper left, displacement field; Lower left, surface pressure; Upper right, strain with* $\alpha = 0.90, \gamma = 0.96$*; Lower right, strain with* $\alpha = 0.70, \gamma = 0.74$*. In the upper left figure the displacement field is shown in the cartesian coordinates* $X$ *and* $Y$ *where the* $X$ *axis is aligned with* $\theta = 0$ *and the* $Y$ *axis is aligned with* $\theta = \pi$*.*

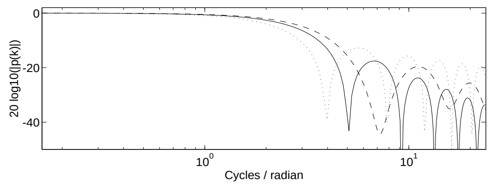


Figure 6: *Fourier coefficients for each indenter type: round (solid line), wedge (dashed line), and punch (dotted line).*

classes. Figure 6 shows a Bode plot of the Fourier coefficients for each of these different indenters. We should note that the ringing in the pressure distribution for the punch contact is an artifact of the truncation of the Fourier series representation of a discontinuous signal. The pressure spectrums do not differ appreciably for spatial frequencies less than 2 cycles/radian. Recalling the Bode plots of the normal strain frequency responses, we see that the spectra of the different indenter classes do not differ appreciably at frequencies below the -20 dB cut-off for the deep sensor. However, the spectra are considerably different in the region of the center frequency of the shallow sensor making discrimination possible.

The similarity of the pressure distributions at the low frequencies can be understood by thinking of the pressure distribution as a periodic shape multiplied by

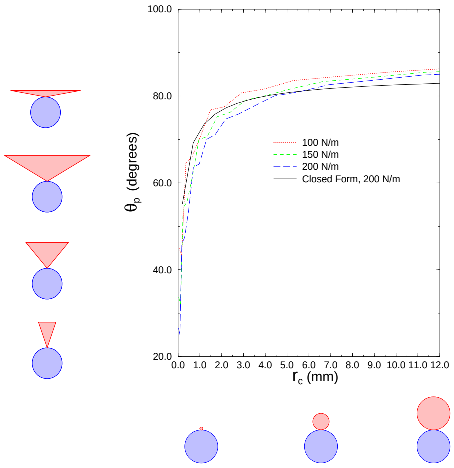


Figure 7: *Wedge angle that has the same contact area for a given radius indenter at a given load.*

a window. In the frequency domain the window will appear as a sinc function. Since in the frequency domain all shapes will have a DC component convolved with the sinc function, the magnitude spectrums will all have a similar shape at the low frequencies. The width of the sinc function in the frequency domain is inversely proportional to the width of the contact, making the contact area the most discernible feature of the surface pressure after contact location and load.

Since we know that indentations with the same contact area are hard to distinguish for deep sensors, it is useful to determine when round and wedge indenters generate the most similar subsurface strain profile. Using the closed form expressions for the pressure distributions of round and wedge indenters, equations (5) and (2) found in the Appendix, one can easily solve for the wedge angle that has the same contact area as a given radius indenter, $r_c$, at a given load, $P$, based on a half plane model.

$$\theta_p = \tan^{-1}\left(\sqrt{\frac{8\mu}{\pi P(1-\sigma)}\frac{r_b r_c}{r_b + r_c}}\right) \tag{1}$$

The closed form solution wedge pressure solution does not include the curvature of the finger nor does the Hertz model account for the rigid core so the equivalent wedge was also computed using pressure distributions generated by the SVD technique [14].

Figure 7 shows the equivalent wedge angle computed by using the SVD method and the closed form model of equation (1). Indenters with an $r_c < 0.5$ mm have the same contact area as that of wedge indenters with $\theta_p < 70^o$. With $r_c > 0.5$mm the equivalent wedge angle asymptotically approaches $90^o$. It appears that there is a useful relation between radius and angle for

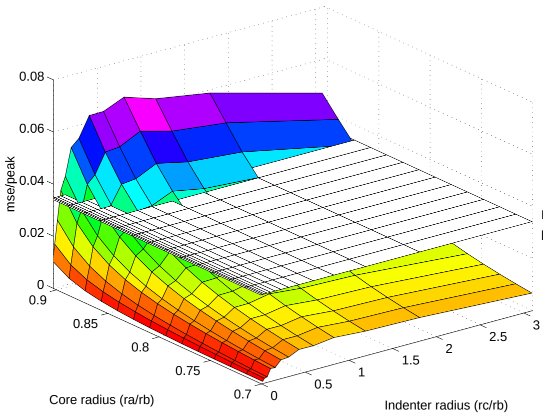


Figure 8: *Standard error as a fraction of peak strain between subsurface normal strains of equivalent wedge and round indenters as a function of indenter radius and sensor depth. Load was held constant at 200 N/m.*

wedge indenters with half angle greater than $70^o$.

To determine when such wedge indenters would be distinguishable from the equivalent radius indenter, the standard error between subsurface strain for equivalent area indenters was computed as a function of sensor depth and equivalent radius as is shown in Figure 8. It is interesting to see that no matter how thin the rubber layer is, when $\frac{r_c}{r_b} < 0.04$, or rather when the wedge angle is less than $70^o$, noise levels would have to be extremely small to discriminate the two indenters. However, when the equivalent radius is the same as the finger radius the two indenter types reach a peak standard error for all sensor depths. As the equivalent radius increases past the finger radius the standard error decreases slowly as both indenters start to look like flat indenters.

A noise plane is shown at the level of 2 standard deviations of typical tactile sensor noise [14]. The intersection of the noise plane with the error surface indicates the boundary of 95 % confidence in classification. It is clear that by lowering the noise level through averaging or better electronics the range of sensor depths and indenter radii over which classification could be achieved will increase quickly due to the low gradient of the error surface. With the current noise level we must have $\alpha > 0.85$ for classification when the equivalent radius, $r_c$, is equal to $r_b$.

### 2.4 Comparison of indenter curvatures

Given that the sensor we will be working with has $\alpha = 0.75$ and we have seen that indenter classification will be difficult in the presence of noise, we should investigate whether different scales of indenter of the same class are distinguishable. In this case we hold the load constant at 200 N/m, but vary the radius of the round indenter to see whether different radii indenters are distinguishable from low frequency information only. In this case we have picked 5 indenters with $r_c \in \{0.5, 1.6, 3.9, 12.3, 25.3\}$ mm. Figure 9 shows the surface displacement, surface stress, and subsurface strains at 2 different depths. Again the Bode plot of the magnitude of the pressure distribution is shown in Figure 10. At 3 cycles/radian the frequency responses are clearly different and should be distinguishable with $\alpha = 0.70$ and a noise level at -40 dB.

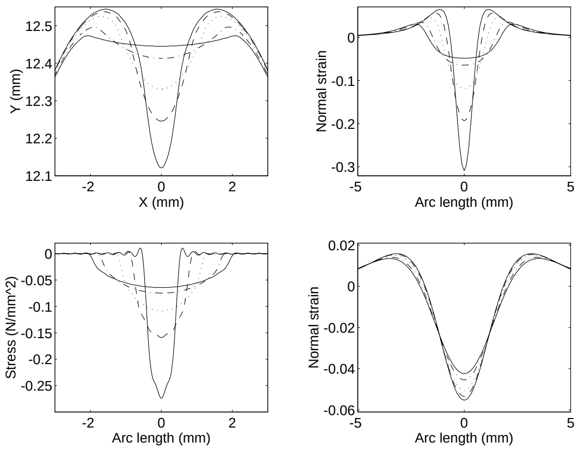


Figure 9: *Comparison of indentation for a fixed load (200 N/m) and varying $r_c \in 0.5, 1.6, 3.9, 12.3, 25.3$. Upper left, displacement field; Lower left, surface pressure; Upper right, strain with $\alpha = 0.70, \gamma = 0.74$; Lower right, strain with $\alpha = 0.90, \gamma = 0.96$. Again the displacement field is in cartesian coordinates.*

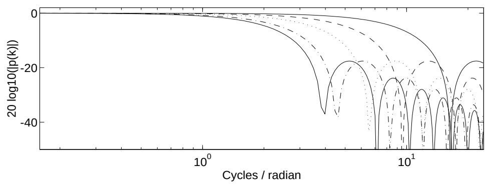


Figure 10: *Fourier coefficients for each indenter radius.*

We can investigate the $r_c$ at which a round indenter can be distinguished from knife edge indenter by plotting the mean square error between the strain profiles at a constant load. If we assume that the sensor noise is gaussian, then the round and edge indenters can be distinguished at a 95 % level when the square root of the mean square error exceeds 2 standard deviations of the noise. Figure 11 shows the error as a function of $r_c/r_b$ and $\alpha = r_a/r_b$. A noise plane is also shown at 2 standard deviations of the typical noise for a tactile sensor. The intersection of the noise plane with

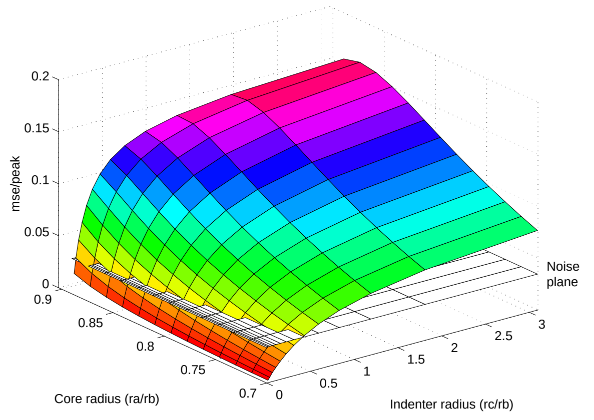


Figure 11: *Standard error as a fraction of peak strain between subsurface normal strains of knife edge and round indenters as a function of indenter radius and sensor depth. Load was held constant at 200 N/m. It is assumed that the strain profile was sampled at a high enough density to be interpolated.*

the error surface gives the boundary at which a round indenter my be distinguished from a knife edge. As would be expected, shallower sensors allow smaller radius indenters to be distinguished from a knife edge. For deep sensors with $\alpha = 0.70$, flat and edge indenters can be distinguished with noise levels as high as 3.7 % of the peak strain. If the noise is as low as 1 % of peak strain then deep sensors can distinguish an indenter with $r_c/r_b = 0.16$ from an edge indenter.

## 3 Conclusions

This paper has sought to provide insight into the problem of determining indenter shape from tactile sensor data. Our approach has been to assume a sensor density, pick a sensor depth based on that density so as not to allow aliasing in the sampled signal, and then to determine the shape sensing capabilities of the sensor. We do not advocate putting the sensors at the surface of the sensor as that will result in a highly aliased sampled signal.

We have seen that deep sensors can allow discrimination of different scales of an indenter class, as has been demonstrated with humans, however classification of indenters requires shallow sensors. The contact area appears to be the most discernible feature of the indentation, after location and load, as it is contained in the low spatial frequencies.

## References


[1] P. R. Basu, R. A. Russell, and G. Trott. Extracting 3-dimensional surface features from tactile sensor data. In *International Symposium and Exposition on Robots*, pages 908–920, Sydney, Australia, Nov. 1988.

[2] A. D. Berger and P. K. Khosla. Using tactile data for real-time feedback. *The International Journal of Robotics Research*, 10(2):88–102, Apr. 1991.

[3] R. E. Ellis and M. Qin. Singular-value and finite-element analysis of tactile shape recognition. In *Proceedings, IEEE International Conference on Robotics and Automation*, pages 2529–2535, San Diego, CA, May 1994.

[4] R. S. Fearing. Tactile sensing mechanisms. *The International Journal of Robotics Research*, 9(3):3–23, June 1990.

[5] R. S. Fearing and T. O. Binford. Using a cylindrical tactile sensor for determining curvature. *IEEE Transactions on Robotics and Automation*, 7(6):806–817, Dec. 1991.

[6] R. S. Fearing and J. M. Hollerbach. Basic solid mechanics for tactile sensing. *The International Journal of Robotics Research*, 4(3):40–54, Fall 1985.

[7] A. W. Goodwin, K. T. John, and A. H. Marceglia. Tactile discrimination of curvature by humans using only cutaneous information from the fingerpads. *Experimental Brain Research*, 86(3):663–672, 1991.

[8] I. E. Gordon and V. Morison. The haptic perception of curvature. *Perception and Psychophysics*, 31(5):446–450, May 1982.

[9] W. D. Hillis. A high-resolution imaging touch sensor. *The International Journal of Robotics Research*, 1(2):33–44, Summer 1982.

[10] B. L. Hutchings, A. R. Grahn, and R. J. Petersen. Multiple-layer cross-field ultrasonic tactile sensor. In *Proceedings, IEEE International Conference on Robotics and Automation*, pages 2522–2528, San Diego, CA, May 1994.

[11] K. L. Johnson. *Contact Mechanics*. Cambridge University Press, Cambridge, England, 1985.

[12] H. Maekawa, K. Tanie, K. Komoriya, M. Kaneko, C. Horiguchi, and T. Sugawara. Development of a finger-shaped tactile sensor and its evaluation by active touch. In *Proceedings, IEEE International Conference on Robotics and Automation*, pages 1327–1334, Nice, France, May 1992.

[13] D. J. Montana. The kinematics of contact with compliance. In *Proceedings, IEEE International Conference on Robotics and Automation*, pages 770–775, Scottsdale, Arizona, May 1989.

[14] E. J. Nicolson. *Tactile Sensing and Control of a Planar Manipulator*. PhD thesis, University of California at Berkeley, Nov. 1994.

[15] E. J. Nicolson and R. S. Fearing. Sensing capabilities of linear elastic cylindrical fingers. In *IEEE/RSJ International Conference on Intelligent Robots and Systems*, pages 178–185, Yokohama, Japan, July 1993.

[16] D. Nowell and D. A. Hills. Tractive rolling of tyred cylinders. *International Journal of Mechanical Sciences*, 30(12):945–957, 1988.

[17] F. Oberhettinger. *Fourier transforms of distributions and their inverses; a collection of tables*. Springer-Verlag, New York, 1990.

[18] D. Reynaerts and H. V. Brussel. Tactile sensing data interpretation for object manipulation. In *Sensors and Acutators A*, pages 268–273, June 1993.

[19] M. Shimojo. Spatial filtering chracteristic of elastic cover for tactile sensor. In *Proceedings, IEEE International Conference on Robotics and Automation*, pages 287–292, San Diego, CA, May 1994.

[20] P. Sikka and H. Zhang. Tactile-assisted robotic object manipulation. In *Fourth International Symposium on Robotics and Manufacturing*, pages 83–88, Santa Fe, New Mexico, 1992. ASME press.

[21] T. H. Speeter. A tactile sensing system for robotic manipulation. *The International Journal of Robotics Research*, 9(6):25–36, Dec. 1990.

# A The Hertz contact

Under the assumption of frictionless contact between a cylinder and an elastic half space the Hertz model predicts an elliptical pressure distribution. (See [11] page 129 and following.) For the contact of a rigid cylinder and and elastic cylinder, the equivalent radius, $R$, may be used. It should be noted that the Hertz assumption is no longer valid for cylinders with a rigid core [16], however when the contact area is small and the elastic layer is thick the approximation is sufficient.

The elliptic pressure distribution is given by

$$p(\theta) = \frac{\mu}{1-\sigma}\left(1+\frac{r_b}{r_c}\right)\left(\left(\frac{\theta_w}{2}\right)^2 - \theta^2\right)^{\frac{1}{2}} \tag{2}$$

where the arc of contact, in radians, $\theta_w$, is given by

$$\theta_w = \frac{2}{r_b}\sqrt{\frac{2P(1-\sigma)}{\pi\mu}\left(\frac{1}{r_b}+\frac{1}{r_c}\right)} \tag{3}$$

and $P$ is the load in N/m.

We can find the Fourier series coefficients for the Hertz contact, defined as

$$\begin{aligned} p_0 &= \frac{1}{2\pi}\int_{-\pi}^{\pi} p(\theta)d\theta \\ p_k^c &= \frac{1}{\pi}\int_{-\pi}^{\pi} p(\theta)\cos k\theta d\theta \\ p_k^s &= \frac{1}{\pi}\int_{-\pi}^{\pi} p(\theta)\sin k\theta d\theta, \end{aligned}$$

at $\theta_c$ from a standard table [17]

$$\begin{aligned} p_0 &= \frac{\mu}{4(1-\sigma)}\left(1+\frac{r_b}{r_c}\right)\left(\frac{\theta_w}{2}\right)^2 \\ p_k^s &= \frac{\mu}{2(1-\sigma)}\left(1+\frac{r_b}{r_c}\right)\left(\frac{\theta_w}{k}\right)J_1\left(\frac{\theta_w}{2}k\right)\sin(k\theta_c) \\ p_k^c &= \frac{\mu}{2(1-\sigma)}\left(1+\frac{r_b}{r_c}\right)\left(\frac{\theta_w}{k}\right)J_1\left(\frac{\theta_w}{2}k\right)\cos(k\theta_c). \end{aligned} \tag{4}$$

where $J_1$ is the Bessel function of the first kind.

## Wedge contact

Johnson [11], page 112, also gives the pressure distribution for a wedge contact on an elastic half-plane as

$$p(\theta) = \frac{2\mu}{\pi(1-\sigma)}\cot\theta_p \cosh^{-1}\left(\frac{\theta_w}{2\theta}\right) \tag{5}$$

where the contact area may be found from

$$\theta_w = P\frac{1-\sigma}{\mu r_b \cot\theta_p}. \tag{6}$$